Chemical Science

ROYAL SOCIETY OF CHEMISTRY

EDGE ARTICLE

View Article Online
View Journal

Cite this: DOI: 10.1039/d5sc08602g

All publication charges for this article have been paid for by the Royal Society of Chemistry

Dopant-free stabilization of ruthenium oxide *via* metallic Ru-induced d-orbital modulation for acidic water electrolysis

Lei Tan,[a] Meharban Faiza,[a] Jin Tian,[a] Lingzhi Zhu,[a] Tiantian Su,[a] Xiaotong Wu,[a] Yujie Song,[a] Qiuju Zhang,[b] Jingsan Xu,[c] Chao Lin,*[a] Xiaopeng Li*[a] and Wei Luo[a]

Proton exchange membrane water electrolysis (PEMWE) is a cornerstone technology for carbon-neutral hydrogen production, yet its scalability is constrained by the intrinsic activity–stability trade-off of oxygen evolution reaction (OER) electrocatalysts. To overcome this challenge, we design a Ru/RuO_2 heterostructure by integrating metallic Ru to modulate the d-orbital electron density of RuO_2. The metallic Ru domains suppress lattice oxygen migration (LOM) while enhancing electron delocalization. The e_g orbital filling shifts the Ru 4d-band center downward, reducing the adsorption strength of reaction intermediates (*OH, *O, and *OOH). The optimized Ru/RuO_2 electrocatalyst achieves an overpotential of 181 mV at 10 mA cm^{-2} in 0.5 M H_2SO_4 and exhibits stable performance for 260 hours with minimal degradation rate (0.065 mV h^{-1}). In the PEMWE device, it lowers the cell voltage from 1.88 V (RuO_2) to 1.68 V (Ru/RuO_2) at 1 A cm^{-2}, exhibiting negligible performance loss over 120 hours. This work introduces a dopant-free electronic engineering strategy that advances the design of stable, high performance pure Ru-based anodic catalysts for energy conversion technologies.

Received 5th November 2025
Accepted 9th January 2026

DOI: 10.1039/d5sc08602g

rsc.li/chemical-science

Introduction

Under the stringent climate mitigation frameworks established by the Intergovernmental Panel on Climate Change (IPCC), carbon-neutral hydrogen has emerged as a critical technology for decarbonizing energy systems to meet the 1.5 °C climate target. Due to its high gravimetric energy density (nearly 3 times higher than gasoline, ~120 MJ kg^{-1}) and ability to store large amounts of clean energy, it plays a vital role in flexible energy storage, grid stabilization, and decarbonization of hard-to-abate sectors, such as heavy industry and long-haul transport.[1–3] Among the available production methods, proton exchange membrane water electrolysis (PEMWE) stands out for its industrial readiness. It combines ultrahigh-purity hydrogen generation (>99.99%, eliminating post-processing) with a rapid dynamic response (<50 ms), enabling seamless coupling with fluctuating renewable inputs. Moreover, PEMWE can achieve near-thermodynamic faradaic efficiencies (>85%) with minimal ohmic losses (<50 m Ω cm^2) even at industrial current densities (>2 A cm^{-2}).[4,5] However, the widespread adoption of PEMWE is hindered by the kinetically demanding oxygen evolution reaction (OER) at the anode, which is a complex four-proton, four-electron transfer process ($2H_2O \rightarrow O_2 + 4H^+ + 4e^-$) and results in substantial overpotential, reducing energy efficiency and increasing system costs.[6,7]

Non-precious metal electrocatalysts, while attractive from a cost perspective, remain fundamentally unsuitable for acidic OER environments. Their intrinsically high activation barriers restrict catalytic turnover, and harsh oxidative conditions of PEMWE (pH < 1, potentials >1.5 V *vs.* RHE) accelerate degradation through metal dissolution, lattice oxygen leaching and surface amorphization.[8–10] This persistent activity–stability trade-off has left iridium-based oxides, particularly IrO_2, as the only commercially deployed OER catalysts for PEMWE, owing to their exceptional durability under acidic conditions.[11,12] However, Ir's geological scarcity (0.001 ppm crustal abundance) and exorbitant cost ($150–200 g^{-1}) render large-scale reliance unsustainable, with iridium contributing over 30% of stack costs. In contrast, RuO_2 offers a compelling alternative, combining superior intrinsic OER activity with a far lower raw material cost (~$16 g^{-1}), positioning it as a promising candidate for cost-effective PEMWE.[13,14] Yet, the practical deployment of RuO_2 is curtailed by its poor durability. At industrially relevant loadings (*e.g.*, 0.4 mg cm^{-2}), RuO_2 catalysts typically fail within 200 hours at 10 mA cm^{-2} due to overoxidation of Ru

[a]State Key Laboratory of Advanced Fiber Materials, College of Materials Science and Engineering, Donghua University, Shanghai 201620, P. R. China. E-mail: linc@dhu.edu.cn; xiaopeng.li@dhu.edu.cn

[b]Key Laboratory of Advanced Fuel Cells and Electrolyzers Technology, Ningbo Institute of Material Technology and Engineering, Chinese Academy of Sciences, Ningbo, Zhejiang, 315201, China

[c]School of Chemistry and Physics & Centre for Materials Science, Queensland University of Technology, Brisbane, QLD 4001, Australia

centers, which initiates lattice collapse, active site dissolution, and cascading catalytic deactivation.[15–17]

Recent strategies to stabilize the RuO_2 electrocatalyst have primarily followed two strategies: metal doping (*e.g.*, Ta, Sn, and Mn) to modulate the electronic structure and suppress overoxidation,[18–23] and heterostructure engineering with acid-resistant supports (*e.g.*, MnO_2 and Co_3O_4) to establish protective electron donor–acceptor networks.[24–27] These approaches aim to shift the reaction pathway from the lattice oxygen mechanism (LOM)—which accelerates lattice degradation—to more robust adsorbate evolution (AEM) or oxide path mechanisms (OPM), while simultaneously mitigating Ru dissolution *via* sacrificial oxidation of dopants or supports. Despite these advances, major challenges remain. Non-precious dopants and supports are themselves prone to acidic dissolution, leading to structural breakdown, whereas inert supports typically exhibit poor conductivity or demand complex syntheses, thereby increasing system costs.[28,29] Consequently, there is an urgent need for intrinsically stable, undoped pure Ru-based electrocatalysts that circumvent reliance on unstable additives.

The stability–activity dilemma of RuO_2 can also be understood through fundamental catalytic design principles. The Sabatier principle emphasizes that optimal activity requires balanced adsorbate binding strength and weak binding hinders activation, whereas strong binding leads to surface passivation by intermediate accumulation.[30] Electronic structure descriptors provide a more quantitative basis for this balance. The d-band center model (E_d)[31,32] and the e_g orbital occupancy framework[33] have emerged as powerful tools to rationalize binding trends in transition-metal catalysts. In transition metal catalysts, the position of the d-band center relative to the Fermi level (E_F) dictates adsorbate binding strength: an E_d near E_F enhances adsorbate stabilization, risking passivation, whereas a downshifted E_d weakens binding, potentially hindering activation.[34] In octahedral coordination environments, common in RuO_2, e_g orbital occupancy fine-tunes reactivity where values below 1 enhance the adsorption of oxygen species (leading to overbinding), while values above 1 weaken essential interactions (impairing activation).[33] Concurrently, increased electron density in the t_{2g} orbitals strengthens Ru–O bonds, enhancing stability by resisting oxidative dissolution.[35] For RuO_2, passivation occurs due to strong adsorption of oxygenated intermediates (O*, OH*, and OOH*) driven by the proximity of E_d to E_F, which increases unoccupied d-orbital character and leads to excessively tight binding, thereby impeding reaction progress.[36,37] These insights underscore a key design challenge of tuning the Ru 4d-band center and modulating e_g/t_{2g} occupancy to simultaneously optimize adsorbate binding strength for high activity and strengthen Ru–O bonds to prevent overoxidation and Ru dissolution.

Recent reports have demonstrated that Ru/RuO_2 heterostructures—synthesized without doping heteroatoms—utilize the work function difference between metallic Ru and RuO_2 to construct a built-in electric field. This field facilitates directional electron transfer from metallic Ru to RuO_2, suppressing the elevation of Ru valence states and the participation of lattice oxygen during acidic OER, thereby enhancing stability.[35,38,39] However, critical research gaps persist in this field: first, the electronic modulation mechanism between Ru and RuO_2 remains insufficiently elucidated; second, the link between Ru-to-RuO_2 electron transfer and adsorption/desorption dynamics of the OER intermediate is still unclear; and third, the durability of such catalysts in practical PEMWE remains unsatisfactory. Herein, we engineered metallic Ru–Ru bonds to precisely modulate the d-orbital electron density of RuO_2, aiming to overcome the long-standing activity–stability trade-off in acidic OER. Density functional theory (DFT) calculations reveal that this electronic modulation induces a controlled downshift of the Ru 4d-band center, weakening the adsorption of oxygenated intermediates (*OH, *O, and *OOH) on the Ru/RuO_2 surface and preventing performance loss from overbinding. Density of states (DOS) analysis demonstrates enhanced electron delocalization across the Ru/RuO_2 interface, which synergistically accelerates OER charge transfer kinetics. Differential electrochemical mass spectrometry (DEMS) confirms that LOM is effectively suppressed in Ru/RuO_2. These synergistic effects translate into exceptional acidic performance, achieving a low overpotential of 181 mV at 10 mA cm^{-2} and maintaining stable operation for 260 hours with a minimal degradation rate of 0.065 mV h^{-1}. When applied in a Ru/RuO_2-based PEMWE system, it operates at 1.68 V at 1.0 A cm^{-2}, with negligible performance loss over 120 hours of continuous operation. By bridging atomic-scale electronic structure engineering with macroscopic catalytic performance, this work establishes a mechanistic framework to overcome the long-standing activity–stability trade-off in acidic OER, advancing the viability of pure Ru-based catalysts for harsh anodic reactions.

Results and discussion

The Ru/RuO_2 electrocatalyst was synthesized through a controlled two-step process to tailor the metallic/oxide interface. In the first step, aqueous $RuCl_3$ was reduced by $NaBH_4$, resulting in a black precipitate of metallic Ru, which was isolated *via* centrifugation, washed, and freeze-dried to yield a fine powder. X-ray diffraction (XRD, Fig. S1) confirmed the formation of the metallic Ru phase (PDF # 06-0663). Transmission electron microscopy (TEM, Fig. S2a) showed these nanoparticles with an average diameter of 2.6 nm (size distribution in Fig. S2b). EDS analysis of metallic Ru nanoparticles (Fig. S3 and Table S2) indicates the presence of an amorphous RuO_x layer on their surface; however, the intense bright contrast of Ru confirms that metallic Ru remains the dominant species. This phenomenon arises from the catalyst's intrinsic structural feature: as a particle-stacked aggregate, the peripherally exposed particles are susceptible to oxidation during synthesis or ambient exposure. In the second step, the Ru nanoparticles underwent controlled annealing at 300 °C in air, partially oxidizing to form the Ru/RuO_2 catalyst. TEM images (Fig. 1a) demonstrated the morphological transformation from Ru nanoparticles (2.6 nm) to larger (~5 nm) particles, with some nanoparticles converted into nanorods exhibiting enhanced crystallinity. High-resolution TEM (HRTEM, Fig. 1b) revealed distinct lattice fringes corresponding to rutile RuO_2, with *d*-

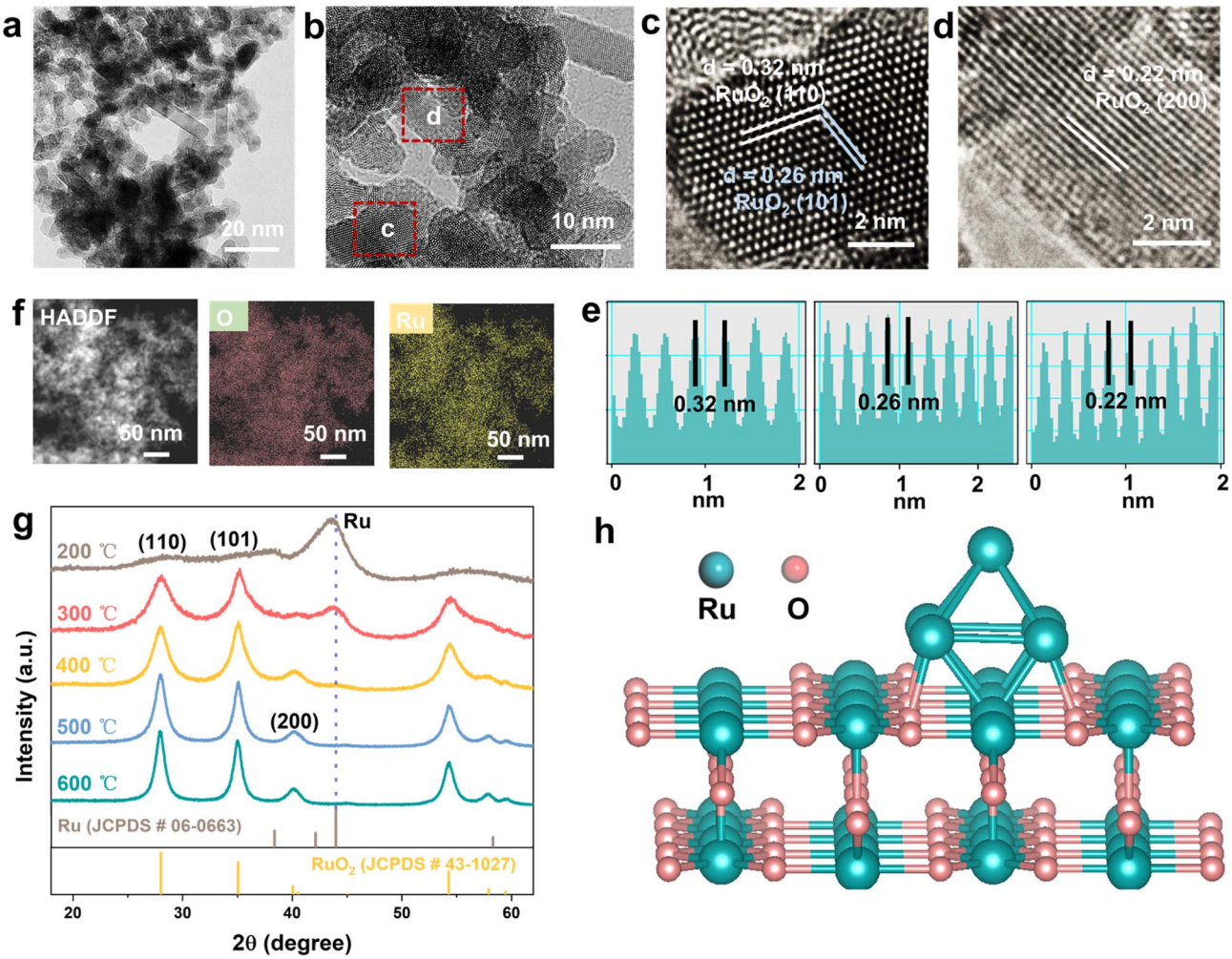

Fig. 1 (a) TEM and (b) HRTEM images of Ru/RuO_2. (c and d) The enlarged areas of pos c, and pos d in (b), respectively. (e) The lattice fringes corresponding to Ru/RuO_2. (f) STEM and EDS mapping images of Ru/RuO_2. (g) The XRD patterns at different annealing temperatures. (h) The front view of Ru/RuO_2 models; Ru atoms are depicted in green, while O atoms are shown in red.

spacings of 0.32, 0.26 and 0.22 nm assigned to the (110), (101) and (200) crystal planes (Fig. 1c–e and S4), respectively. Energy-dispersive X-ray spectroscopy (EDS) mapping (Fig. 1f) confirmed homogeneous distribution of Ru and O elements. Systematic optimization of the annealing temperature (Fig. 1g) revealed distinct phase behaviors. At 200 °C, metallic Ru remained the dominant phase but exhibited structural instability in acidic electrolytes. XRD analysis of the sample annealed at 300 °C (Ru/RuO_2) confirmed the retention of the rutile RuO_2 structure, with a weak (101) diffraction peak indicating the presence of metallic Ru. Notably, the characteristic diffraction peak of metallic Ru gradually weakens with increasing annealing temperature. The complete oxidation to RuO_2 was achieved when temperature exceeded up to 500 °C. Therefore, controlling the calcination temperature within an appropriate range was crucial for the formation of the Ru/RuO_2 heterostructure (Fig. 1h). Nitrogen physisorption isotherms of Ru/RuO_2 (Fig. 2a) and RuO_2 (Fig. 2b) displayed Type IV profiles with H3 hysteresis loops, typical of mesoporous structures formed by particle aggregation. Brunauer–Emmett–Teller (BET) analysis revealed a specific surface area of 84.3 $m^2\ g^{-1}$ for Ru/RuO_2, nearly double that of RuO_2 (43.8 $m^2\ g^{-1}$). Pore size distribution showed a narrow peak at 2.16 nm for Ru/RuO_2, compared to a broader distribution with an average of 3.05 nm for RuO_2. Both materials feature pores that exceed the critical size (0.35 nm) required for efficient O_2 diffusion.[40]

To investigate the local atomic environments of Ru/RuO_2, Ru K-edge extended X-ray absorption fine structure (EXAFS) spectroscopy was employed, with Ru foil and RuO_2 as references. The Fourier-transformed EXAFS (FT-EXAFS) spectrum of Ru/RuO_2 (Fig. 2c) displays a dominant first-shell peak at ~1.45 Å, corresponding to octahedrally coordinated Ru–O bonds in the rutile RuO_2 phase.[41] A secondary peak at ~2.41 Å, matching the Ru–Ru metallic bonding feature in Ru foil confirms the presence of metallic Ru domains. In addition, the peak located at ~3.11 Å corresponds to the Ru–O–Ru bridging bonds in RuO_2, which is consistent with the RuO_2 EXAFS feature. The coexistence of these distinct peaks further verifies the heterostructural nature of Ru/RuO_2. Wavelet transform (WT) analysis enhances k-space resolution and revealed three distinct oscillatory

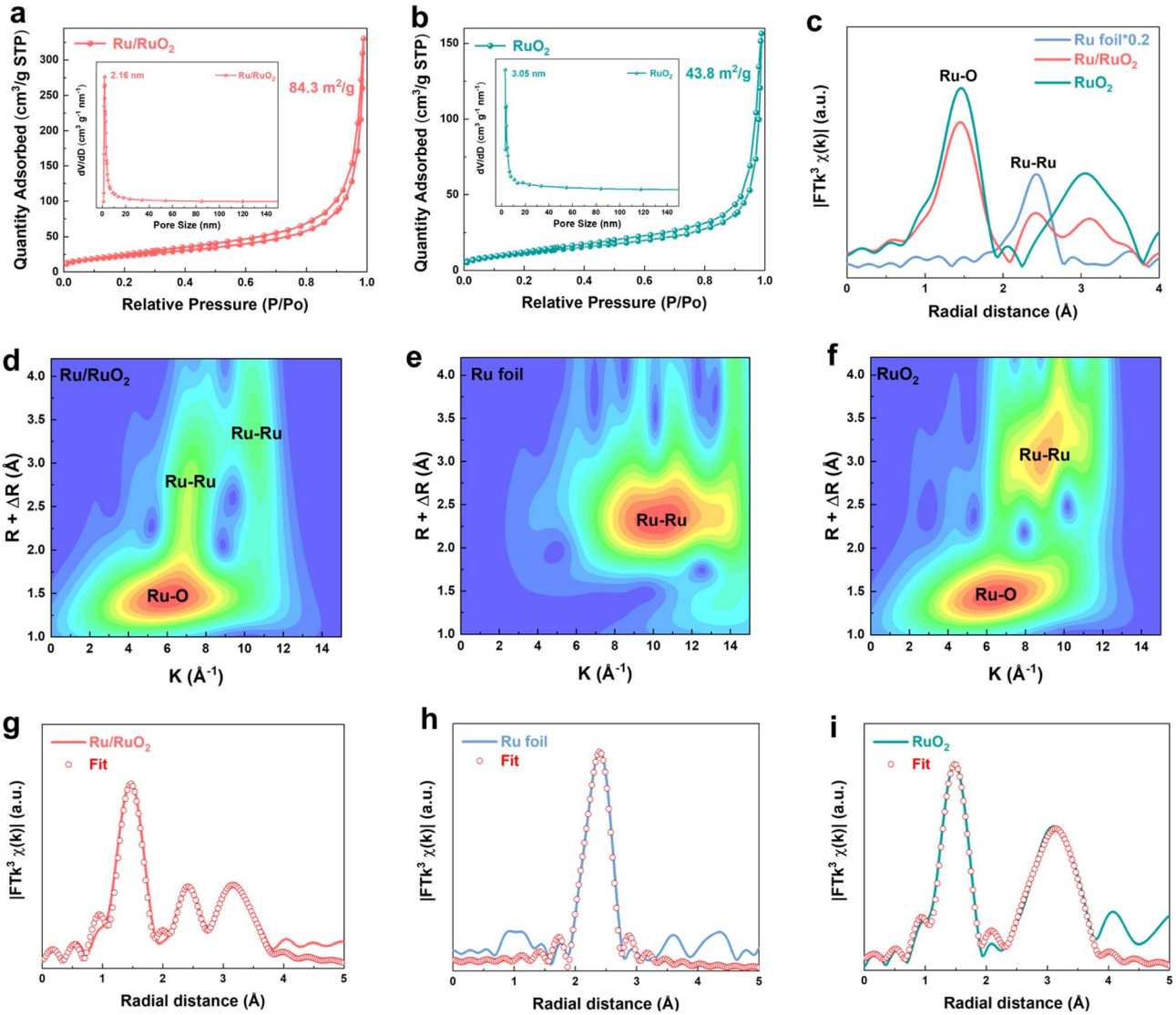

Fig. 2 N_2 adsorption/desorption isotherms and pore size distribution of (a) Ru/RuO_2, and (b) RuO_2. (c) k^3-weighted Fourier transforms of Ru K-edge EXAFS for Ru foil, Ru/RuO_2, and RuO_2. Wavelet transforms for (d) Ru/RuO_2, (e) Ru foil, and (f) RuO_2. Ru K-edge EXAFS fitting analyses for (g) Ru/RuO_2, (h) Ru foil, and (i) RuO_2.

regions in Ru/RuO_2 (Fig. 2d),[42] corresponding to metallic Ru (Fig. 2e) and RuO_2 (Fig. 2f), which support the coexistence of two phases in the heterostructure. Quantitative EXAFS fitting in both k- and R-space (Fig. 2g–i and S5) revealed key structural features in Ru/RuO_2 (Table S1). The coexistence of Ru–O and Ru–Ru bonding environments directly confirms the heterostructure. Ru–O bonds (coordination number ~5.6) indicate preserved RuO_2 domains, while Ru–Ru bonds (coordination number ~2.1) verify metallic Ru phases. Notably, Ru–O and Ru–Ru bond lengths remain unchanged from parent phases.

Ru K-edge X-ray absorption near-edge spectroscopy (XANES) was employed to investigate the electronic structure of Ru/RuO_2 (Fig. 3a). The XANES spectrum of Ru/RuO_2 closely resembles that of RuO_2 but exhibits a K-edge half-peak energy shift lower than that of RuO_2 (+4 oxidation state) and higher than that of Ru foil (0 oxidation state). Quantitative analysis (Fig. 3b) reveals an average Ru valence of +3.81 in Ru/RuO_2, situated between that of RuO_2 and Ru foil. X-ray photoelectron spectroscopy (XPS) further provided the information about the surface oxidation states (Fig. S6). The Ru(IV) $3d_{5/2}$ peak in Ru/RuO_2 at 280.95 eV is positioned between RuO_2 (281.09 eV) and metallic Ru (280.30 eV) (Fig. 3c), aligning with high-resolution Ru 3d curve-fitting[43,44] (Fig. S7). Soft X-ray absorption spectroscopy (SXAS) at the Ru M_3-edge provides atomic-level validation of interfacial charge transfer. The M_3-edge transition ($3p_{3/2}$ to 4d) in Ru/RuO_2 occurs at 463.0 eV, 0.2 eV lower than RuO_2 (463.2 eV) and 0.8 eV higher than metallic Ru (462.2 eV) (Fig. 3d),[45] confirming a reduced oxidation state relative to RuO_2. O K-edge X-ray absorption spectroscopy (XAS) was used to probe the Ru 4d electronic structure in Ru/RuO_2 and RuO_2 (Fig. 3e). The spectrum is anchored by the O 1s core-level peak at 530 eV (red), with the occupied states consisting of hybridized Ru (green) and O

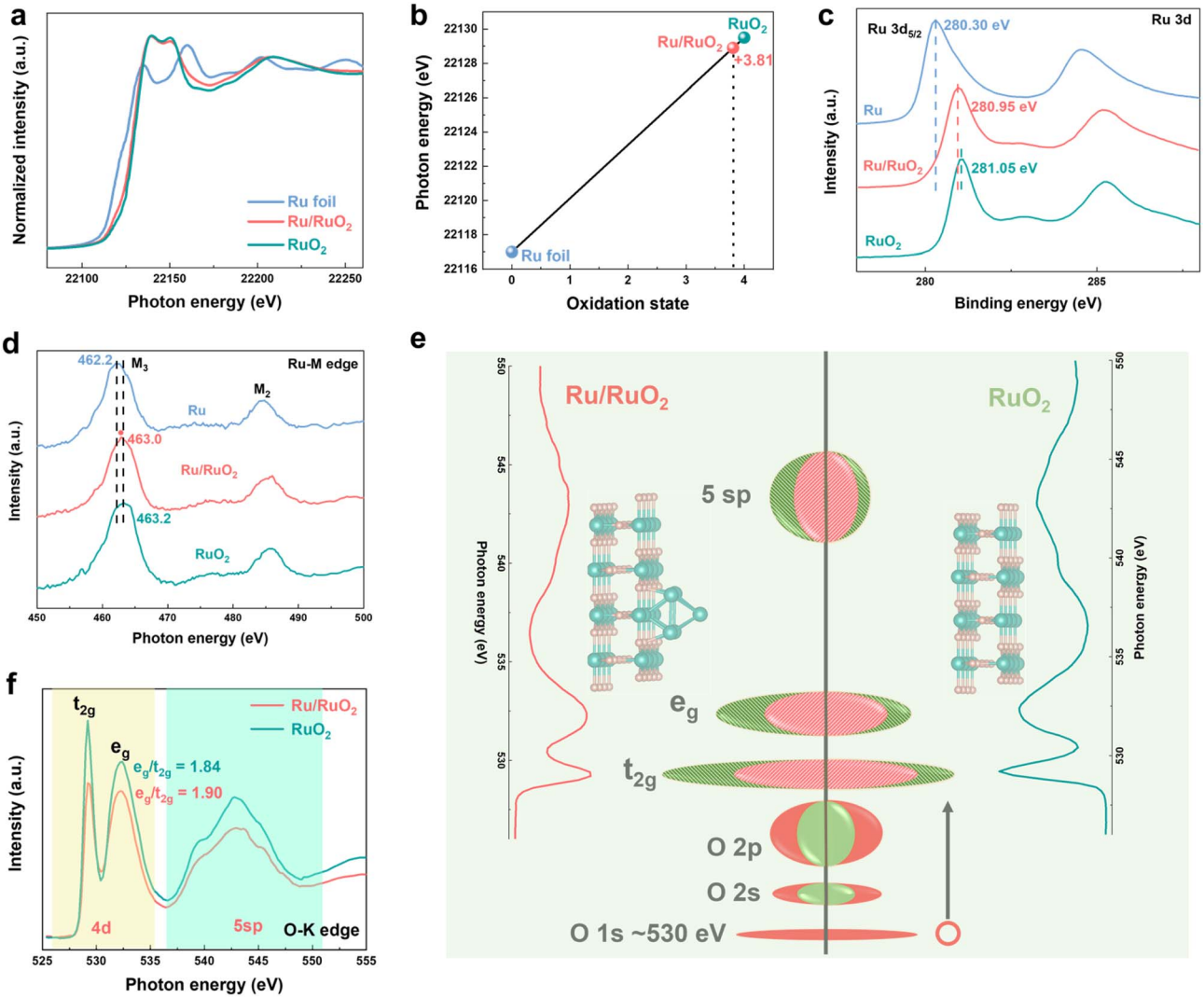

Fig. 3 (a) Ru K-edge XANES spectra and (b) derived oxidation states. (c) XPS spectra of Ru 3d for metallic Ru, Ru/RuO_2, and RuO_2. (d) The XAS spectra of the Ru M-edge for metallic Ru, Ru/RuO_2, and RuO_2. (e) Interpretation of O K-edge XAS for the Ru 4d electronic structure of Ru/RuO_2 and RuO_2. The O 1s core state is given in red at a binding energy of 530 eV. The occupied O 2s and 2p bands are given as a combination of O (red) and Ru (green). The empty states are given with striped colors: the ratio of t_{2g} and e_g states is 6 : 4, but the O contribution (in red) is equivalent. At higher energy, the metal 5 sp band is given. Variations in the overlap regions of these spectral bands reflect changes in the degree of orbital hybridization between the constituent species. (f) O K-edge spectra of Ru/RuO_2 and RuO_2.

2s/2p bands. Under crystal field splitting, two distinct absorption features emerge at 529.2 eV and 532.2 eV, which are attributed to the transitions of O 1s electrons to hybridized O 2p-Ru 4d t_{2g} and e_g orbitals, respectively.[46] Empty states (striped colors) exhibit a t_{2g} : e_g ratio of 6 : 4, with O character equivalently distributed between the two-orbital sets. This directly reflects covalent interactions between these two elements. In contrast, metallic Ru lacks these features and exhibits a significant shift, arising from delocalized free electrons (Fig. S8). Notably, Ru/RuO_2 displays reduced e_g and t_{2g} feature intensities relative to RuO_2, indicating a lower degree of O 2p-Ru 4d hybridization,[46,47] indicative of increased electron occupancy in these orbitals.[48–51] The e_g/t_{2g} ratio increases from 1.84 (RuO_2) to 1.90 (Ru/RuO_2) (Fig. 3f), signifying preferential filling of the lower-energy t_{2g} orbitals. This enhanced t_{2g} electron density strengthens Ru–O covalent bonding, possibly suppressing oxidative dissolution and improving thermodynamic stability.[35] A broader feature at 542.8 eV corresponds to O 2p-Ru 5 sp hybrid transitions.

The OER performance of RuO_2-based catalysts annealed at various temperatures was systematically evaluated using a three-electrode system in 0.5 M H_2SO_4 electrolyte. Linear sweep voltammetry (LSV) (Fig. S9) revealed that Ru/RuO_2 (annealed at 300 °C), a hybrid catalyst comprising both metallic Ru and RuO_2 phases, demonstrates superior catalytic activity. The comparison of LSV curves for Ru/RuO_2, RuO_2, and commercial RuO_2 (Com. RuO_2) (Fig. 4a) demonstrates that Ru/RuO_2 requires overpotentials of 181 mV, 226 mV, and 250 mV to achieve current densities of 10 mA cm^{-2}, 50 mA cm^{-2}, and 100 mA cm^{-2}, respectively (Fig. S10). These values represent

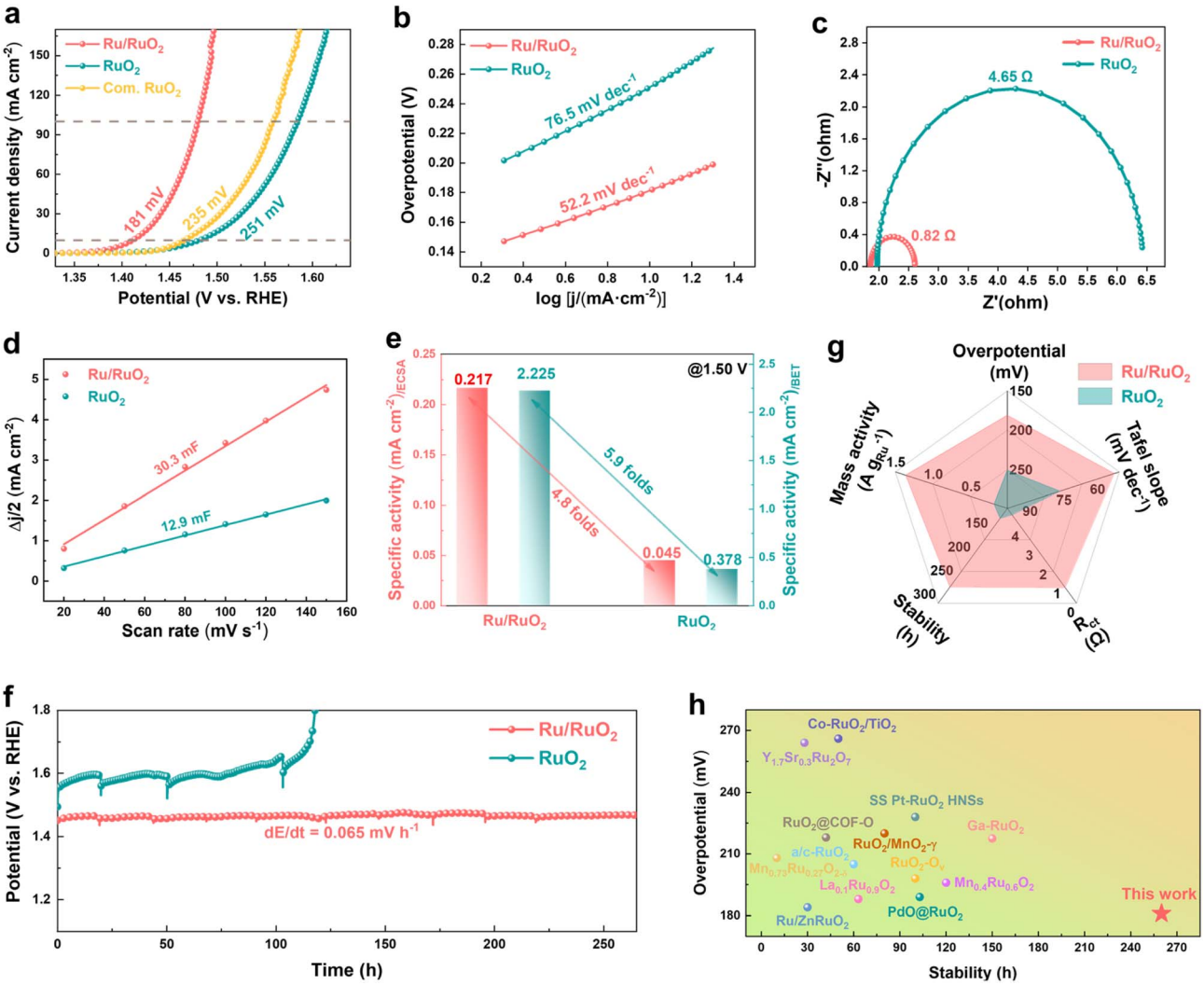

Fig. 4 (a) LSVs of Ru/RuO_2, RuO_2, and Com. RuO_2 in 0.5 M H_2SO_4. (b) The Tafel plots of Ru/RuO_2 and RuO_2. (c) The EIS of Ru/RuO_2 and RuO_2. (d) The C_{dl} of Ru/RuO_2 and RuO_2. (e) The specific OER activity normalized by BET surface area and ECSA for Ru/RuO_2 and RuO_2. (f) The chronopotentiometry curves for Ru/RuO_2 and RuO_2 at a current density of 10 mA cm^{-2}. (g) Comparison of the overpotentials, Tafel slopes, mass activity, stability, and R_{ct} of Ru/RuO_2 with RuO_2. (h) Comparison of the overpotentials and stability slopes for Ru/RuO_2 with several reported advanced RuO_2-based OER electrocatalysts.

substantial reductions in overpotentials: 70 mV, 92 mV, and 105 mV compared to RuO_2, and 54 mV, 69 mV, and 79 mV relative to Com. RuO_2. Kinetic analysis further supports the superior performance of Ru/RuO_2, with a Tafel slope of 52.2 mV dec^{-1}, significantly lower than that of RuO_2 (76.5 mV dec^{-1}) (Fig. 4b), indicating accelerated reaction kinetics for the OER. Electrochemical impedance spectroscopy (EIS) (Fig. 4c) provided additional insights into charge transport properties. Ru/RuO_2 exhibits a solution resistance (R_s) of 1.86 Ω, slightly lower than that of RuO_2 (1.97 Ω), confirming its favorable electrical conductivity. More critically, Ru/RuO_2 shows a significantly reduced charge transfer resistance (R_{ct} = 0.82 Ω) compared to RuO_2 (4.65 Ω), which is direct evidence of improved electron transfer at the catalyst–electrolyte interface. Cyclic voltammetry (CV) measurements (Fig. S11a and b) were employed to quantify the electrochemically active surface area (ECSA) *via* double-layer capacitance (C_{dl}) analysis. Ru/RuO_2 exhibits a C_{dl} of 30.3 mF, nearly 2.4 times that of RuO_2 (12.9 mF) (Fig. 4d), corresponding to a larger ECSA (866 cm^2 *vs.* 368 cm^2 for RuO_2) (Fig. S11c). To isolate the intrinsic catalytic efficiency from extrinsic factors (*e.g.*, surface area and metal loading), specific OER performance was normalized using three key parameters: BET surface area (Fig. S12a), ECSA (Fig. S12b), and Ru mass loading (Fig. S12c and Table S2). Across all normalized metrics, Ru/RuO_2 consistently outperforms RuO_2 (Fig. 4e), confirming that the improved performance stems from enhanced intrinsic catalytic efficiency at the active site level, rather than mere surface area effects. Electrochemical stability was evaluated *via* long-term chronopotentiometry at a constant current density of 10 mA cm^{-2}. Ru/RuO_2 showed exceptional stability, with an overpotential increase rate of only 0.065 mV h^{-1} over a 260-hour test (Fig. 4f), significantly outperforming RuO_2 under identical conditions.

Notably, even when the current density was increased to 50 mA cm^{-2}, its stability remained notably superior to that of RuO_2 under the same testing parameters (Fig. S13). After 2000 CV cycles, only a marginal potential drop of 10 and 15 mV was observed at 10 and 100 mA cm^{-2}, respectively (Fig. S14), underscoring its exceptional durability. Benchmarking against the established literature further demonstrated that Ru/RuO_2 ranks among the most competitive OER catalysts, exhibiting superior activity and stability to both homemade RuO_2 (Fig. 4g) and other advanced RuO_2-based catalysts (Fig. 4h and Table S3).

To elucidate the enhanced stability of Ru/RuO_2, XRD, EXAFS, and XPS were employed to characterize structural and electronic evolution of Ru/RuO_2 after stability analysis. The Ru/RuO_2-spent and RuO_2-spent samples correspond to the catalysts (1 mg cm^{-2} mass loading on carbon paper) following 10 h of stable operation at 50 mA cm^{-2} (Fig. S13). XRD analysis (Fig. 5a) showed new diffraction peaks beyond the background signal from the carbon paper substrate, confirming the absence of phase transitions or the formation of new crystalline phases. FT-EXAFS (Fig. 5b) further validated this stability, showing negligible shifts in the bond distances of Ru–O, Ru–Ru, and Ru–O–Ru, with minimal variations in CN for these configurations (Fig. S15 and Table S4). These findings collectively affirm the preservation of both the local atomic structure and long-range order, underscoring the structural integrity of Ru/RuO_2 after prolonged OER operation. Electronic stability was investigated through Ru K-edge XANES and XPS. XANES spectra (Fig. 5c) displayed no positive shift in the absorption edge, ruling out significant oxidation state changes of Ru during the reaction. Complementary XPS analysis (Fig. 5d) revealed negligible variations in the binding energies of the Ru $3d_{5/2}$ and Ru $3d_{3/2}$ peaks for Ru/RuO_2-spent compared to the fresh catalyst. Collectively,

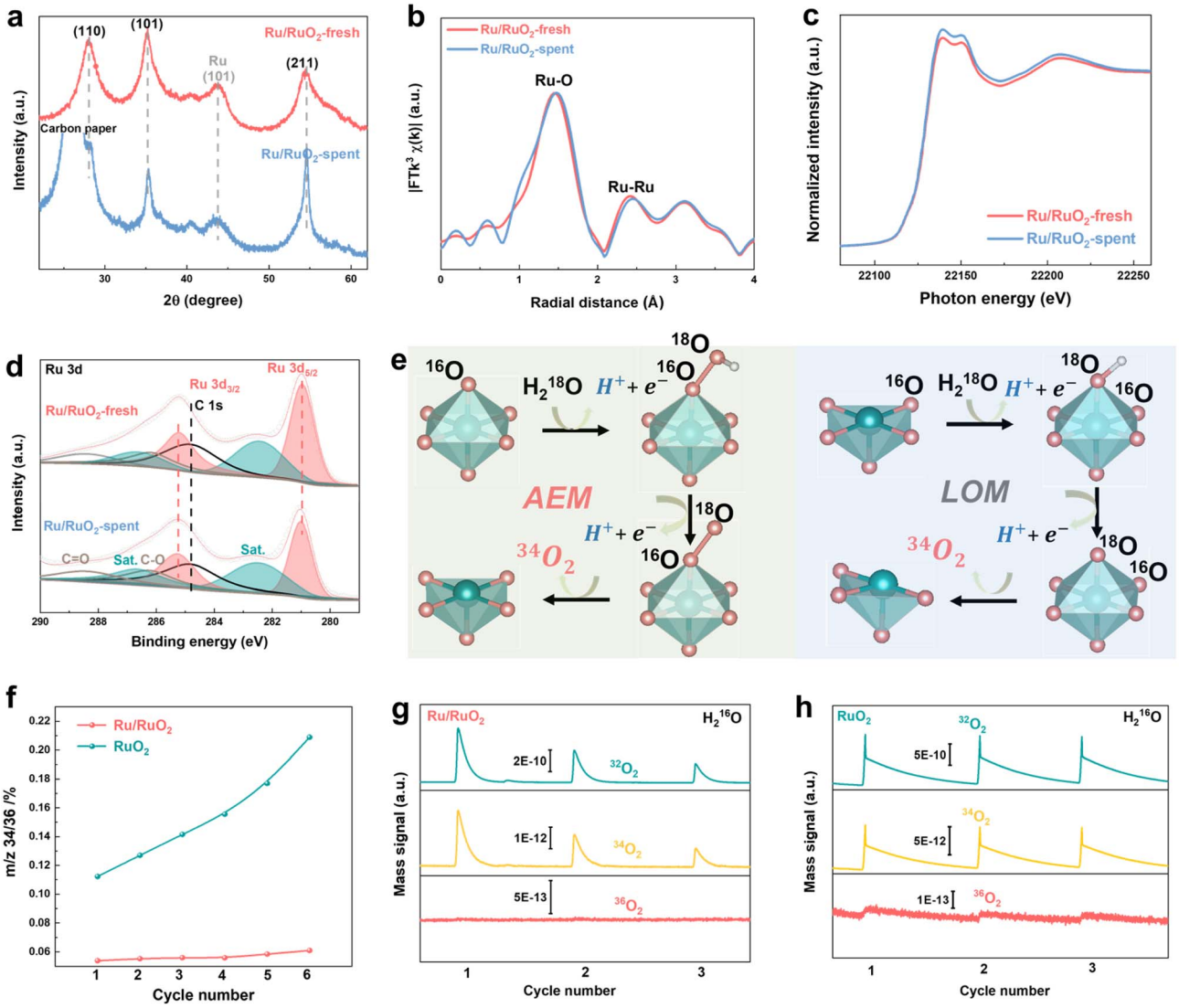

Fig. 5 (a) The XRD patterns of Ru/RuO_2-fresh and Ru/RuO_2-spent. (b) FT-EXAFS and (c) XANES spectra at the Ru K-edge for Ru/RuO_2-fresh and Ru/RuO_2-spent. (d) High-resolution XPS spectra of Ru 3d of Ru/RuO_2-fresh and Ru/RuO_2-spent. (e) Schematic illustration of $^{34}O_2$ evolution pathways in $H_2{}^{18}O$ electrolyte solvent. (f) $^{34}O_2/^{36}O_2$ signal intensity ratios for Ru/RuO_2 and RuO_2 derived from DEMS measurements. DEMS spectra of ^{18}O-labeled (g) Ru/RuO_2 and (h) RuO_2.

these results confirm that the electronic structure of Ru/RuO_2 remains stable under OER conditions. In stark contrast, to elucidate the root cause of the RuO_2 control sample's suboptimal performance, we performed comprehensive XRD and XPS characterization of pristine RuO_2 before and after long-term stability testing (Fig. S16). XRD analysis showed negligible crystal structure perturbations post-testing, whereas XPS detected a distinct positive shift of Ru core-level peaks to higher binding energies, indicative of elevated Ru oxidation states. This oxidation state elevation provides a compelling mechanistic rationale for the RuO_2 control's marked performance degradation under prolonged OER conditions.

Operando differential electrochemical mass spectrometry (DEMS) with isotope labeling was employed to investigate the OER mechanism. During repeated LSV cycles using $H_2{}^{18}O$ electrolyte (Fig. S17 and S18), mass signals corresponding to $^{34}O_2$ and $^{36}O_2$ were detected for both catalysts (Fig. S19). The dominance of $^{36}O_2$, a characteristic signature of the adsorbate evolution mechanism (AEM), confirms AEM as the primary pathway for the OER on both materials.[52] The $^{34}O_2$ signals, which may originate from either AEM (*via* surface-adsorbed oxygen) or lattice oxygen-mediated mechanism (LOM, involving catalyst lattice oxygen), serves as a critical indicator of lattice oxygen participation (Fig. 5e).[53–55] Specifically, the $^{34}O_2/^{36}O_2$ intensity ratio directly quantifies the extent of lattice oxygen involvement, providing a metric for assessing catalytic stability. Over six consecutive LSV cycles, Ru/RuO_2 exhibited minimal variation in the $^{34}O_2/^{36}O_2$ ratio (0.05 to 0.06), whereas RuO_2 showed a pronounced increase (0.11 to 0.21; Fig. 5f). This divergence indicates that Ru/RuO_2 exhibits superior stability

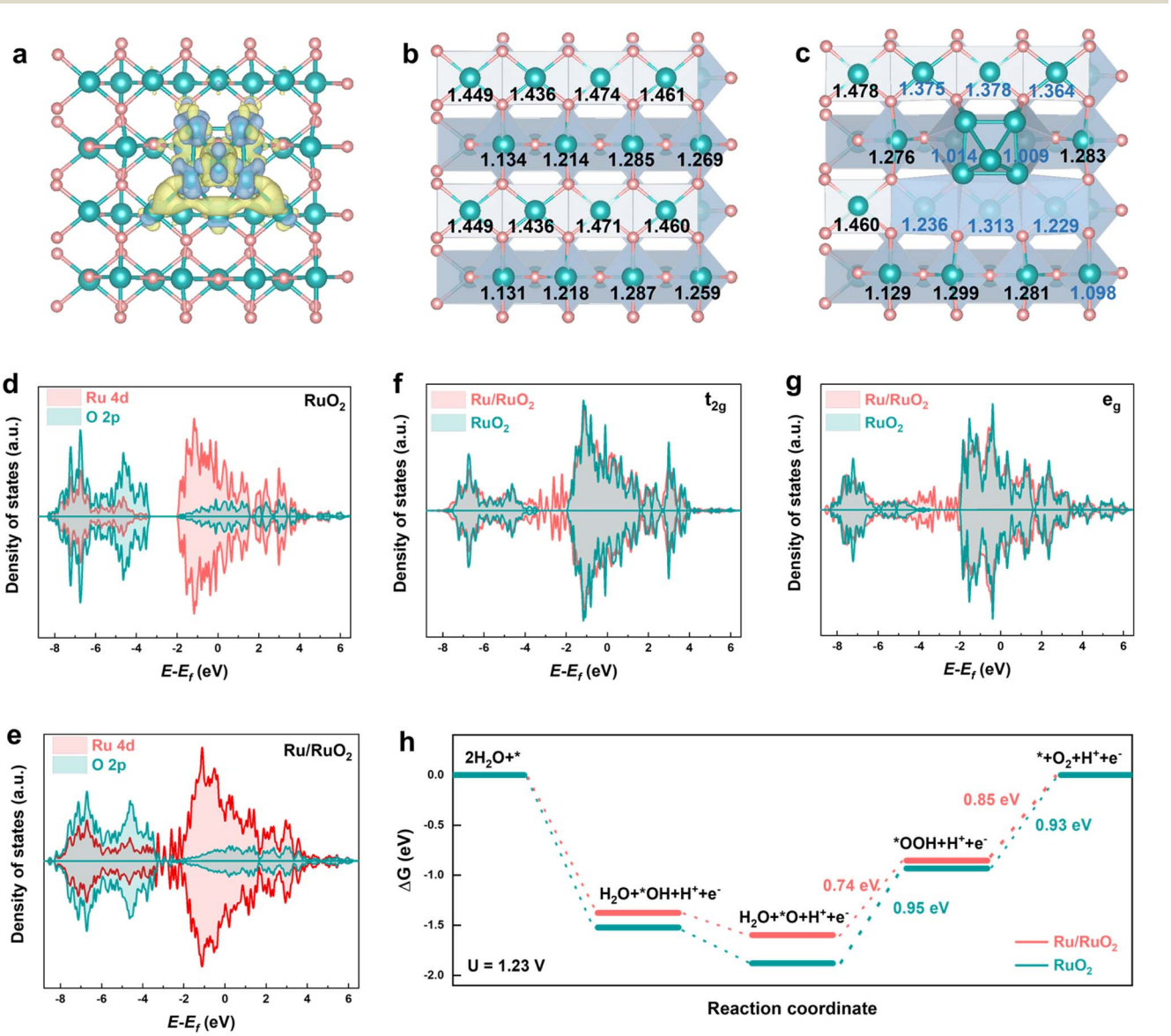

Fig. 6 (a) Differential charge density of Ru/RuO_2. Yellow and blue contours represent the charge accumulation and depletion, respectively. (green: Ru, red: O). Bader charge results of (b) RuO_2 and (c) Ru/RuO_2. The PDOS for Ru 4d and O 2p of (d) RuO_2 and (e) Ru/RuO_2. The orbital-resolved PDOS in (f) t_{2g} and (g) e_g for RuO_2 and Ru/RuO_2. (h) Gibbs free energy profiles for the OER steps of RuO_2 and Ru/RuO_2.

with negligible lattice oxygen involvement, while RuO_2 experiences lattice oxygen engagement, which is linked to its stability degradation.[56] Complementary experiments with ^{18}O-labeled catalysts in $H_2{}^{16}O$ electrolyte further corroborated these findings (Fig. S20 and S21). ^{18}O-labeled Ru/RuO_2 only produced $^{34}O_2$ and $^{32}O_2$ signals (Fig. 5g), confirming that the OER process relies exclusively on surface-adsorbed oxygen. In contrast, ^{18}O-labeled RuO_2 exhibited a weak but detectable $^{36}O_2$ signal (Fig. 5h), conclusively demonstrating the incorporation of lattice oxygen into the evolved O_2. These results reveal that the enhanced stability of Ru/RuO_2 arises from the suppression of the LOM pathway, while the instability of RuO_2 is driven by progressive lattice oxygen loss and concomitant structural degradation.

To elucidate the underlying mechanism responsible for the superior OER performance of Ru/RuO_2 relative to RuO_2, we performed systematic density functional theory (DFT) calculations. Models of rutile RuO_2 (Fig. S22 and Table S5) and Ru/RuO_2 (Fig. S23 and Table S6) were constructed and geometrically optimized, ensuring structural validity with lattice parameters and bond lengths consistent with experimental date. The differential charge density map reveals significant charge redistribution at the interface between metallic Ru and RuO_2 (Fig. 6a and S24). Bader charge analysis quantifies these perturbations; as compared to RuO_2 (Fig. 6b and Table S7), in Ru/RuO_2, the metallic Ru loses 0.80 electrons, while adjacent O atoms lose 0.26 electrons (Table S8). Conversely, Ru cations in the oxide phase gain 1.06 electrons, with the largest electron accumulation localized on oxidized Ru species near the metallic Ru domains (Fig. 6c). To further explore orbital-dependent changes, projected density of states (PDOS) calculations were conducted for both systems. RuO_2 exhibits a semiconductor-like band structure with a distinct band gap (Fig. 6d), while Ru/RuO_2 shows enhanced electron delocalization and elimination of the band gap (Fig. 6e). Orbital-resolved PDOS analysis reveals increased electron occupancy in both the t_{2g} (Fig. 6f) and e_g (Fig. 6g) orbitals of Ru/RuO_2, consistent with experimental observations from O K-edge XAS (Fig. 3f). Notably, d-band center analysis shows that the Ru 4d-band center of Ru/RuO_2 (−1.236 eV) is downshifted relative to RuO_2 (−1.175 eV) (Table S9), weakening the adsorption strength of reaction intermediates.[34] Collectively, these electronic modifications, including optimized orbital occupancy and modulated intermediate binding, provide a foundational rationale for the improved catalytic performance of Ru/RuO_2 in the OER.[57–59] Gibbs free energy (ΔG) profiles further validated the thermodynamic advantages of Ru/RuO_2 (Fig. 6h). Relative to RuO_2, Ru/RuO_2 weakens the adsorption of oxygenated intermediates, reducing the energy barrier for the *O → *OOH step from 0.95 eV (RuO_2) to 0.74 eV (Ru/RuO_2). Concomitantly, the RDS shifts from the *O → *OOH transformation to O_2 desorption, with the desorption energy barrier notably reduced from 0.93 eV (RuO_2) to 0.85 eV (Ru/RuO_2).

To evaluate the real-world performance of the Ru/RuO_2 catalyst, a single-cell PEMWE device was assembled with Ru/RuO_2 as the anode catalyst and commercial 60% Pt/C as the cathode (Fig. 7a), utilizing a Hyproof HPM-2080X perfluorosulfonic acid membrane as the proton conductor. Specifically, the mass loadings of both the anode and cathode catalysts in the PEMWE device are ~2 mg cm^{-2}. Polarization tests

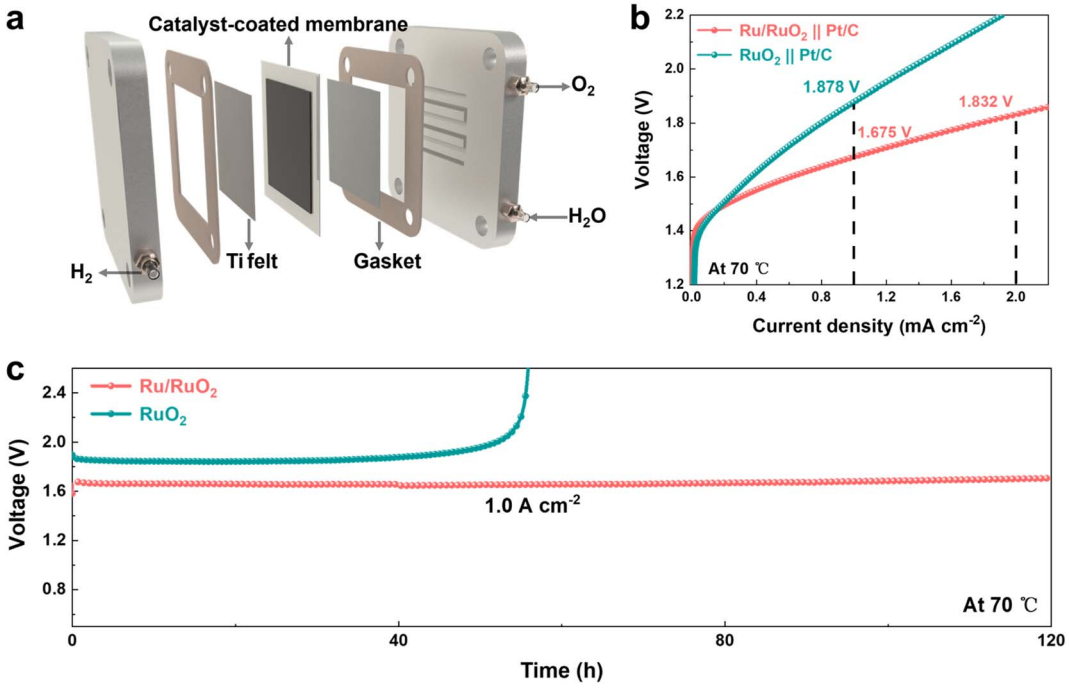

Fig. 7 (a) Schematic of the PEMWE device. (b) Polarization curves for the PEMWE of Ru/RuO_2 and RuO_2 at 70 °C. (c) Chronopotentiometry curves for Ru/RuO_2 and RuO_2 at a current density of 1 A cm^{-2}.

conducted at 70 °C demonstrated that the Ru/RuO_2-based electrolyzer achieved a current density of 1 A cm^{-2} at a cell voltage of 1.68 V, whereas the RuO_2 control required 1.88 V to reach the same current density under identical operating conditions (Fig. 7b). Critical for industrial scalability, long-term durability testing of the Ru/RuO_2-based PEMWE device revealed stable operation at 1 A cm^{-2} over 120 hours of continuous electrolysis, with negligible voltage fluctuations and no signs of accelerated degradation. In stark contrast, RuO_2 catalysts underwent significant performance deactivation within just 60 hours under identical testing conditions (Fig. 7c). Systematic benchmarking against state-of-the-art RuO_2-based electrocatalysts reported recently demonstrates that the Ru/RuO_2 heterostructure holds notable performance merits, ranking favorably alongside other advanced counterparts in key OER metrics including activity and long-term stability (Table S10). These results confirm that the enhanced activity and stability of Ru/RuO_2 are driven by tailored d-orbital tuning and heterostructure which translate to practical electrolyzer performance, positioning it as a robust candidate for scalable, energy-efficient carbon-neutral hydrogen production.

Conclusions

In conclusion, we present a strategy for modulating the d-orbital electron density of RuO_2 through the integration of metallic Ru. DFT calculations and O K-edge XAS data demonstrate that this approach effectively lowers the d-band center of Ru/RuO_2 while simultaneously enhancing the t_{2g}/e_g orbital occupancy ratio. This modulation weakens the binding strength of oxygenated intermediates, thereby reducing the passivation risk of RuO_2 caused by excessively strong adsorption of these intermediates. DEMS data further confirm the significant suppression of the LOM mechanism, a key degradation pathway for RuO_2, thus enhancing catalyst stability. These synergistic electronic effects result in outstanding acidic OER activity and stability, without the need for dopants or supportive substrates. Specifically, the optimized Ru/RuO_2 catalyst achieves a 70-mV overpotential reduction at 10 mA cm^{-2} and exhibits stable operation for 260 hours with a minimal degradation rate of 0.065 mV h^{-1}. In PEMWE devices, Ru/RuO_2-based electrodes reduce cell voltage from 1.88 V (RuO_2) to 1.68 V at 1 A cm^{-2}, with negligible degradation over 120 hours. This work establishes a paradigm for electronic structure engineering in pure Ru systems, where precise d-orbital and interfacial modulation simultaneously addresses activity–stability trade-offs in acidic OER. By avoiding unstable dopants, this strategy advances fundamental understanding of Ru-based catalysis and enables its practical application in harsh anode environments.

Author contributions

X. L. and C. L. conceived the project. L. T. prepared the samples and measured their electrochemical performance. J. T., L. Z., T. S., X. W., and Y. S. collected the experimental characterization data. L. T. performed the DFT calculations. C. L., X. L., and L. T. wrote and revised the manuscript with the help of all authors. M. F, Q. Z., J. X. and W. L. helped with the manuscript revision.

Conflicts of interest

The authors declare no competing financial interest.

Data availability

The data supporting this article have been included as part of the supplementary information (SI). The data that support the findings of this study are available from the corresponding authors upon reasonable request. Supplementary information: supplementary materials and electrochemical characterization results including experiment section, XRD pattern, TEM images, EXAFS fitting analyze, XPS spectra, XAS spectra, DEMS results, electrochemical performance curves, comparison with previous works, and details of DFT calculation. See DOI: https://doi.org/10.1039/d5sc08602g.

Acknowledgements

This work was supported by the National Natural Science Foundation of China (W2511047, 52272289, 52402231, 52225204, and 52173233), the Innovation Program of Shanghai Municipal Education Commission (2021-01-07-00-03-E00109), the Shanghai Scientific and Technological Innovation Project (24520712800), AI-Enhanced Research Program of shanghai Municipal Education Commission (SMEC-AI-DHUZ-04), the Program for Professor of Special Appointment (Eastern Scholar) at Shanghai Institutions of Higher Learning, Natural Science Foundation of Shanghai (23ZR1479200), the Fundamental Research Funds for the Central Universities and the DHU Distinguished Young Professor Program. We thank BL02B and BL20U in the Shanghai Synchrotron Radiation Facility, and BL01B of the Hefei Synchrotron Radiation Laboratory.

References

1 A. Odenweller and F. Ueckerdt, *Nat. Energy*, 2025, **10**, 110–123.
2 J. Turner, *Science*, 2004, **305**, 972–974.
3 N. Johnson, M. Liebreich, D. Kammen, P. Ekins, R. McKenna and I. Staffell, *Nat. Rev. Clean Technol.*, 2025, **1**, 351–371.
4 H. Tao, H. Liu, K. Lao, Y. Pan, Y. Tao, L. Wen and N. Zheng, *Nat. Nanotechnol.*, 2024, **19**, 1074–1076.
5 L. King, M. Hubert, C. Capuano, J. Manco, N. Danilovic, E. Valle, T. Hellstern, K. Ayers and T. Jaramillo, *Nat. Nanotechnol.*, 2019, **14**, 1071–1074.
6 L. Seitz, C. Dickens, K. Nishio, Y. Hikita, J. Montoya, A. Doyle, C. Kirk, A. Vojvodic, H. Hwang, J. Nørskov and T. Jaramillo, *Science*, 2016, **353**, 1011–1014.
7 X. Zhang, Y. Zhang, B. Protsenko, M. Soldatov, J. Zhang, C. Yang, S. Bo, H. Wang, X. Chen, C. Wang, W. Cheng and Q. Liu, *Nat. Commun.*, 2025, **16**, 6921.
8 R. Wan, T. Yuan, L. Wang, B. Li, M. Liu and B. Zhao, *Nat. Catal.*, 2024, **7**, 1288–1304.

9 A. Martín, S. Mitchell, C. Mondelli, S. Jaydev and J. Pérez-Ramírez, *Nat. Catal.*, 2022, **5**, 854–866.
10 D. Simondson, M. Tesch, I. Spanos, T. Jones, J. Guo, B. Kerr, M. Chatti, S. Bonke, R. Golnak, B. Johannessen, J. Xiao, D. MacFarlane, R. Hocking and A. Simonov, *Nat. Energy*, 2025, **10**, 1013–1024.
11 X. Han, T. Mou, S. Kang, A. Islam, X. Zhao, K. Sasaki, J. Rodriguez, Q. Chang, P. Liu and J. Chen, *Angew. Chem., Int. Ed.*, 2025, **64**, e202507468.
12 C. Yang, Y. Zhu, F. Zhang, L. Yao, Y. Chen, T. Lu, Q. Li, J. Li, G. Wang, Q. Cheng and H. Yang, *Adv. Mater.*, 2025, **37**, 2507560.
13 N. Danilovic, R. Subbaraman, K. Chang, S. Chang, Y. Kang, J. Snyder, A. Paulikas, D. Strmcnik, Y. Kim, D. Myers, V. Stamenkovic and N. Markovic, *J. Phys. Chem. Lett.*, 2014, **5**, 2474–2478.
14 A. Bertelsen, M. Kløve, N. Broge, M. Bondesgaard, R. Stubkjær, A. Dippel, Q. Li, R. Tilley, M. Jørgensen and B. Iversen, *J. Am. Chem. Soc.*, 2024, **146**, 23729–23740.
15 Z. Wu, F. Chen, B. Li, S. Yu, Y. Finfrock, D. Meira, Q. Yan, P. Zhu, M. Chen, T. Song, Z. Yin, H. Liang, S. Zhang, G. Wang and H. Wang, *Nat. Mater.*, 2023, **22**, 100–108.
16 N. Yao, H. Jia, J. Zhu, Z. Shi, H. Cong, J. Ge and W. Luo, *Chem*, 2023, **9**, 1882–1896.
17 Y. Mu, J. Fan, T. Gao, L. Wang, L. Zhang, X. Zou, W. Zheng, Y. Zhang, Z. Yu and X. Cui, *Angew. Chem., Int. Ed.*, 2025, **64**, e202504876.
18 X. Jiang, J. Zhu, M. Jiang, P. Zhang, W. Wen, W. Cai, Y. Ding, P. Sun and M. Cao, *Adv. Mater.*, 2025, **37**, 2503354.
19 J. Zhang, X. Fu, S. Kwon, K. Chen, J. Yang, T. Uchiyama, Y. Uchimoto, S. Li, Y. Li, X. Fan, F. Xia, J. Wu, Y. Li, Q. Yue, L. Qiao, D. Su, H. Zhou, W. Goddard III and Y. Kang, *Science*, 2025, **387**, 48–55.
20 L. Deng, S. Hung, S. Liu, S. Zhao, Z. Lin, C. Zhang, Y. Zhang, A. Wang, H. Chen, J. Peng, R. Ma, L. Jiao, F. Hu, L. Li and S. Peng, *J. Am. Chem. Soc.*, 2024, **146**, 23146–23157.
21 L. Tan, X. Wu, H. Wang, J. Zeng, B. Mei, X. Pan, W. Hu, M. Faiza, Q. Xiao, Y. Zhao, C. Fu, C. Lin, X. Li and W. Luo, *ACS Catal.*, 2024, **14**, 11273–11285.
22 L. Wu, W. Huang, D. Li, H. Jia, B. Zhao, J. Zhu, H. Zhou and W. Luo, *Angew. Chem., Int. Ed.*, 2025, **64**, e202413334.
23 J. Chen, J. Ma, T. Huang, Q. Liu, X. Liu, R. Luo, J. Xu, X. Wang, T. Jiang, H. Liu, Z. Lv, T. Yao, G. Wang, X. Zheng, Z. Li and W. Chen, *Angew. Chem., Int. Ed.*, 2025, **64**, e202503330.
24 R. Deng, F. Liu, S. Gao, Z. Xia, R. Wu, J. Kong, J. Yang, J. Wen, X. Zhang, C. Lv, Y. Wang, X. Li and Z. Wang, *ACS Catal.*, 2025, **15**, 1782–1794.
25 Z. Li, H. Sheng, Y. Lin, H. Hu, H. Sun, Y. Dong, X. Chen, L. Wei, Z. Tian, Q. Chen, J. Su and L. Chen, *Adv. Funct. Mater.*, 2024, **34**, 2409714.
26 M. Huo, H. Sun, Z. Jin, W. Liu, Y. Liang, J. Liu, C. Liu, Z. Xing, Y. Yang and J. Chang, *J. Am. Chem. Soc.*, 2025, **147**, 10678–10689.
27 S. Zuo, Z. Wu, D. Xu, R. Ahmad, L. Zheng, J. Zhang, L. Zhao, W. Huang, H. Qahtani, Y. Han, L. Cavallo and H. Zhang, *Nat. Commun.*, 2024, **15**, 9514.
28 L. Wang, S. Hung, S. Zhao, Y. Wang, S. Bi, S. Li, J. Ma, C. Zhang, Y. Zhang, L. Li, T. Chen, H. Chen, F. Hu, Y. Wu and S. Peng, *Nat. Commun.*, 2025, **16**, 3502.
29 S. Zhao, S. Hung, Y. Wang, S. Li, J. Yang, W. Zeng, Y. Zhang, H. Chang, H. Chen, F. Hu, L. Li and S. Peng, *J. Am. Chem. Soc.*, 2025, **147**, 7993–8003.
30 M. Che, *Catal. Today*, 2013, **218**, 162–171.
31 B. Hammer and J. Nørskov, *Nature*, 1995, **376**, 238–240.
32 A. Vojvodic, J. Nørskov and F. Abild-Pedersen, *Top. Catal.*, 2014, **57**, 25–32.
33 J. Suntivich, K. May, H. Gasteiger, J. Goodenough and Y. Shao-Horn, *Science*, 2011, **334**, 1383–1385.
34 S. Sun, X. Zhou, B. Cong, W. Hong and G. Chen, *ACS Catal.*, 2020, **10**, 9086–9087.
35 Q. Lu, J. Liu, X. Zou, B. Huang, W. Wu, J. Yin, Z. Liu and Y. Wang, *Angew. Chem., Int. Ed.*, 2025, **64**, e202503733.
36 I. Man, H. Su, F. Calle-Vallejo, H. Hansen, J. Martínez, N. Inoglu, J. Kitchin, T. Jaramillo, J. Nørskov and J. Rossmeisl, *Chemcatchem*, 2011, **3**, 1159–1165.
37 L. Yang, R. Grzeschik, S. Schlücker and W. Xie, *Chem. Eur J.*, 2024, **30**, e202401718.
38 Y. Song, W. Zhao, Z. Wang, W. Shi, F. Zhang, Z. Wei, X. Cui, Y. Zhu, T. Wang, L. Sun and B. Zhang, *J. Am. Chem. Soc.*, 2025, **147**, 13775–13783.
39 G. Zhao, W. Guo, M. Shan, Y. Fang, G. Wang, M. Gao, Y. Liu, H. Pan and W. Sun, *Adv. Mater.*, 2024, **36**, 2404213.
40 S. Chen, H. Huang, P. Jiang, K. Yang, J. Diao, S. Gong, S. Liu, M. Huang, H. Wang and Q. Chen, *ACS Catal.*, 2020, **10**, 1152–1160.
41 X. Duan, N. Wen, S. Liu, H. Li, X. Jiao, D. Chen and Y. Xia, *ACS Catal.*, 2025, **15**, 10119–10129.
42 H. Funke, A. Scheinost and M. Chukalina, *Phys. Rev. B*, 2005, **71**, 094110.
43 J. Bai, L. Cheng, S. Liu, H. Zhang, Y. Lian, Y. Deng, Q. Zhou, Y. Tang and Y. Su, *Appl. Surf. Sci.*, 2024, **642**, 158613.
44 J. Chen, Y. Ma, T. Huang, T. Jiang, S. Park, J. Xu, X. Wang, Q. Peng, S. Liu, G. Wang and W. Chen, *Adv. Mater.*, 2024, **36**, 2312369.
45 M. Retuerto, L. Pascual, F. Calle-Valleji, P. Ferrer, D. Gianolio, A. Pereira, A. Garcia, J. Torreor, M. Fernández-Díaz, P. Bencok, M. Peña, J. Fierro and S. Rojas, *Nat. Commun.*, 2019, **10**, 2041.
46 F. Frati, M. Hunault and F. Groot, *Chem. Rev.*, 2020, **120**, 4056–4110.
47 H. Tsai, P. Babu, C. Pao, J. Chiou, J. Jan, K. Krishna-Kumar, F. Chien, W. Pong, M. Tsai, C. Chen, L. Jang, J. Lee, R. Chen, Y. Huang and D. Tsai, *Appl. Phys. Lett.*, 2007, **90**, 042108.
48 X. Miao, L. Zhang, L. Wu, Z. Hu, L. Shi and S. Zhou, *Nat. Commun.*, 2019, **10**, 3809.
49 J. Zhou, H. Fang, Y. Hu, T. Sham, C. Wu, M. Liu and F. Li, *Phys. Chem. C*, 2009, **113**, 10747–10750.
50 H. Zhong, X. Wang, G. Sun, Y. Tang, S. Tan, Q. He, J. Zhang, T. Xiong, C. Diao, Z. Yu, S. Xi, W. Lee and J. Xue, *Energy Environ. Sci.*, 2023, **16**, 641–652.
51 H. Zhong, Q. Zhang, J. Yu, X. Zhang, C. Wu, H. An, Y. Ma, H. Wang, J. Zhang, Y. Zhang, C. Diao, Z. Yu, S. Xi, X. Wang and J. Xue, *Nat. Commun.*, 2023, **14**, 7488.

52 W. Zheng, Y. Zhao, K. Jiang, F. Xie, L. Meng, S. Gao, J. Li, J. Lan, M. Luo, L. Liu and Y. Tan, *Nat. Commun.*, 2025, **16**, 6716.
53 H. Wang, C. Lin, L. Tan, J. Shen, X. Wu, X. Pan, Y. Zhao, H. Zhang, Y. Sun, B. Mei, H. Um, Q. Xiao, W. Jiang, X. Li and W. Luo, *Nat. Commun.*, 2025, **16**, 3976.
54 X. Wang, W. Pi, Z. Li, S. Hu, H. Bao, W. Xu and N. Yao, *Nat. Commun.*, 2025, **16**, 4845.
55 J. Chen, Y. Ma, C. Cheng, T. Huang, R. Luo, J. Xu, X. Wang, T. Jiang, H. Liu, S. Liu, T. Huang, L. Zhang and W. Chen, *J. Am. Chem. Soc.*, 2025, **147**, 8720–8731.
56 X. Cao, L. Miao, W. Jia, H. Qin, G. Lin, R. Ma, T. Jin and L. Jiao, *Nat. Commun.*, 2025, **16**, 6217.
57 H. Do and J. Lee, *ACS Nano*, 2022, **16**, 17847–17890.
58 G. Fan, H. Sun, F. Cheng and J. Chen, *Sci. Sin.: Chim.*, 2019, **49**, 741–751.
59 J. Chen, A. Millis and C. Marianetti, *Phys. Rev. B*, 2015, **91**, 241111.